Investigation of Magnetic Field Immunity and Near Magnetic Field Reduction for the Inductors in High Power Density Design

Yanwen Lai, Shuo Wang, *Senior Member, IEEE*, and Boyi Zhang, *Student Member, IEEE*

***Abstract*—This paper investigates the magnetic field immunity and near magnetic field reduction for different inductor-winding structures. A double-twisted winding structure, which includes two magnetic cores, is proposed for common mode (CM) inductors. The proposed CM inductor can achieve much lower near magnetic field emission, much better magnetic field immunity against the external magnetic field, and much bigger differential mode (DM) impedance than conventional winding structures. The proposed inductor structures are good for high power-density applications. Theoretical analysis, magnetic three-dimensional simulations and experiments were conducted to validate the developed theory and technique.**

***Index Terms*—Induced noise voltage, near magnetic field emission, near magnetic field immunity, winding structure.**

I. Introduction

ELECTROMAGNETIC interference (EMI) has become an increasingly important issue in high power density power electronics system design, especially with the employment of wide bandgap (WBG) devices, which significantly increase switching frequencies [21]. As one of the most widely used components in power electronics devices, inductors play an important role in EMI emission and suppression. In high power density power electronics systems, components are very close to each other [18], which will give rise to EMI issues due to near magnetic field couplings. The components in limited space will cause interference to each other via near field couplings [6]. For instance, when the current with high frequency and high ripples flows through the resonant inductor of an LLC resonant converter, the inductor can generate significant time-varying leakage magnetic field. The leakage magnetic field can couple to other devices and filter components, inducing additional power loss [22] and EMI noise. The filter inductors of photovoltaic inverters using a WBG device can also generate significant near magnetic field emissions due to the high-frequency and high-magnitude noise current flowing through inductors. The emitted

Manuscript received April 30, 2018; revised July 15, 2018; accepted August 20, 2018. Date of publication September 4, 2018; date of current version April 20, 2019. This work was supported by the National Science Foundation under Grant 1540118. Recommended for publication by Associate Editor F. Costa. *(Corresponding author: Shuo Wang.)*

The authors are with the Department of Electrical and Computer Engineering, University of Florida, Gainesville, FL 32611-6200, USA (e-mail:

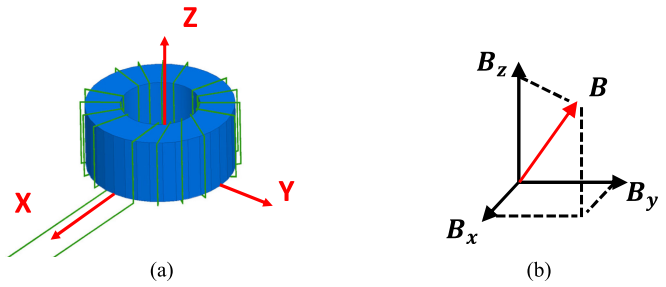

Fig. 1. (a) Single-ended inductor at the origin of an *xyz* coordinate. (b) Decomposing magnetic field to *x*-, *y*-, and *z*-components.

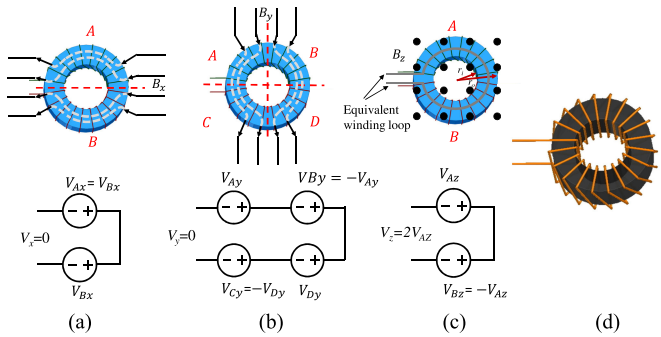

Fig. 2. Induced voltages in a single-ended inductor's winding within (a) magnetic field in the *x*-direction, (b) magnetic field in the *y*-direction, (c) magnetic field in the *z*-direction, and (d) structure of an inductor with a single-ended winding.

II. Induced Noise Voltages in the External Magnetic Field

A. Inductor With Single-Ended Windings

The single-ended winding structure is commonly used in toroidal inductors. An inductor with single-ended winding structure is at the origin of an *xyz* coordinate in Fig. 1. An even and time-varying magnetic field ***B(t)*** in an arbitrary direction can always be decomposed to components $\boldsymbol{B_x(t)}$, $\boldsymbol{B_y(t)}$, and $\boldsymbol{B_z(t)}$ in *x*-, *y*-, and *z*-directions, respectively, as given in Fig. 1(b). When an inductor is within ***B(t)***, the induced noise voltage within the inductor windings can be analyzed separately for *xyz* components based on the superposition theory.

It is assumed that the winding turns are evenly distributed on the inductor core. Because the inductor cores have much higher permeability, they will possess much lower reluctance and magnetic motive force (MMF) than air, and when the magnetic flux penetrates the surface of the core, it is perpendicular to the surface as shown in Fig. 2. Due to the low reluctance of the core, the magnetic flux flows inside along the core as shown in Fig. 2. In Fig. 2(a), for $\boldsymbol{B_x(t)}$ component, the induced noise voltages V_{Ax} and V_{Bx} within the two inductor winding halves have the same magnitude, but reverse polarities in the winding, so they cancel each other. As a result, the induced voltage is $V_x = 0$. For $\boldsymbol{B_y(t)}$ in Fig. 2(b), the winding is separated into four equal winding parts. The induced noise voltages V_{Ay} and V_{By} in the winding parts A and B have the same magnitude, but reverse polarities, so they cancel each other. The induced noise voltages V_{Cy} and V_{Dy} in winding parts C and D have the same magnitude, but reverse polarities, so they cancel each other too. Because of this, the total induced voltage V_y is zero. As shown in Fig. 2(c), due to the round shape of the toroidal core, the winding along the core forms an equivalent winding loop with a radius approximately equal to the core's mean radius. $\boldsymbol{B_z(t)}$ induces a nonzero noise voltage V_z in this equivalent winding loop as shown in Fig. 2(c). The induced voltage V_z is given by

$$V_Z = V_{Az} - V_{Bz} = 2V_{Az} = \pi\left(\frac{r_o + r_i}{2}\right)^2 \frac{dB_z(t)}{dt} \quad (1)$$

where r_o and r_i are the outer and inner radii of the core, respectively. In summary, for a conventional inductor with a single-ended winding structure, if the winding turns are evenly distributed along the core, the induced noise voltage is due to the *z*-direction external magnetic field, and its magnitude is proportional to the area of this equivalent winding loop.

This means that the toroidal inductors with larger radii tend to have higher induced noise voltages and they are more sensitive to the *z*-direction external magnetic field than those with smaller radii. To reduce the induced noise voltage, the *z*-direction magnetic field should be avoided.

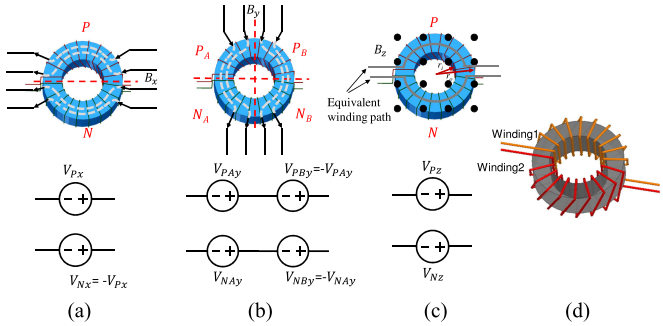

Fig. 3. Induced voltages in a conventional CM inductor's windings within (a) magnetic field in the *x*-direction, (b) magnetic field in the *y*-direction, (c) magnetic field in the *z*-direction, and (d) structure of a conventional CM inductor with balanced two windings.

B. Conventional CM Inductor With Balanced Two Windings

A conventional CM inductor has a balanced two-winding structure as shown in Fig. 3. Each winding of P and N occupies half of the core, and all winding turns are evenly distributed along the core. When two windings carry currents with the same magnitude and direction, the magnetic flux generated by the two windings is added inside the core. When the CM inductor is within an even and time-varying magnetic field ***B(t)***, the induced voltage can be analyzed for *xyz* components separately in Fig. 3.

In Fig. 3(a), there are induced voltages V_{Px} and V_{Nx} in windings P and N for the *x*-component of the magnetic field $\boldsymbol{B_x(t)}$. The induced CM voltage $V_{\mathrm{CM}x}$ and DM voltage $V_{\mathrm{DM}x}$ within two windings are defined by (2). The CM and DM voltages are defined based on the definition on line impedance stabilization networks, which were used for EMI measurement. Because V_{Px} and V_{Nx} have the same magnitude, but inverse polarities, the total induced $V_{\mathrm{CM}x}$ is 0 and the total induced DM voltage $2V_{\mathrm{DM}x}$ across the two windings is twice that of the induced voltage in each winding as given by (3). For the $\boldsymbol{B_y(t)}$ component in

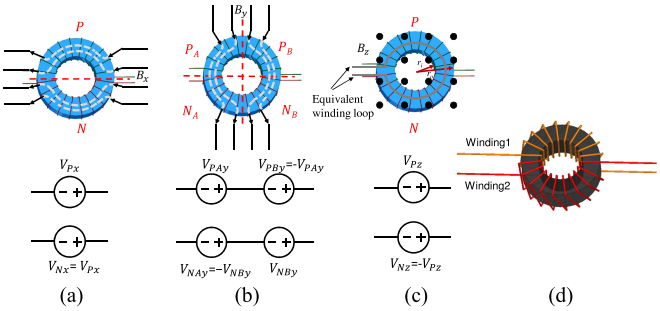

Fig. 4. Induced voltages in a balanced two-winding DM inductor within (a) magnetic field in the *x*-direction, (b) magnetic field in the *y*-direction, (c) magnetic field in the *z*-direction, and (d) structure of a balanced two-winding DM inductor.

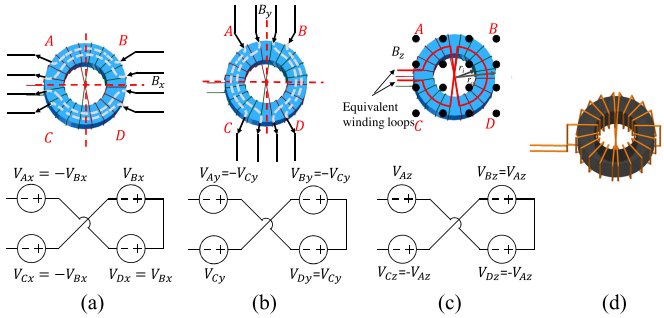

Fig. 5. Induced voltages in an inductor with single twisted winding within (a) magnetic field in the *x*-direction, (b) magnetic field in the *y*-direction, (c) magnetic field in the *z*-direction, and (d) structure of an inductor with a single twisted winding.

Fig. 3(b), the induced noise voltages V_{PAy} and V_{PBy} in the two winding halves P_A and P_B, respectively, and the induced noise voltages V_{NAy} and V_{NBy} in two winding halves N_A and N_B, respectively, cancel out, so the induced noise voltages in both windings are zero. For the $\boldsymbol{B_z(t)}$ component in Fig. 3(c), because the induced noise voltages V_{Pz} and V_{Nz} in the two windings are a function of loop areas determined by the equivalent winding paths in Fig. 3(c) and the returning paths (not shown in the figure), the induced voltages depend on the actual PCB layout. The induced noise voltage includes both CM $V_{\mathrm{CM}z}$ and DM voltage $V_{\mathrm{DM}z}$ given by (4). The total induced DM voltage across the two windings is $2V_{\mathrm{DM}z}$ in (5)

$$V_{CMx} = \frac{V_{Px} + V_{Nx}}{2} = 0, V_{DMx} = \frac{V_{Px} - V_{Nx}}{2} \tag{2}$$

$$2V_{DMx} = V_{Px} - V_{Nx} = 2V_{Px} \tag{3}$$

$$V_{CMz} = \frac{V_{Pz} + V_{Nz}}{2}, V_{DMz} = \frac{V_{Pz} - V_{Nz}}{2} \tag{4}$$

$$2V_{DMz} = V_{Pz} - V_{Nz}\,. \tag{5}$$

The above-mentioned analysis indicates that the conventional CM inductors are sensitive to both *x*- and *z*-direction external magnetic fields. To reduce the induced voltages, the inductor should be orientated, so the external magnetic field is from the *y*-direction, and the two returning paths should be very close to the two equivalent winding paths, so $V_{\mathrm{CM}z}$ and $V_{\mathrm{DM}z}$ can be minimized.

C. DM Inductor With Balanced Two Windings

A balanced two-winding DM inductor is shown in Fig. 4. Different from the regular DM inductor in Section II-A, it has two directly coupled windings and four terminals. It can provide a high DM inductance due to the two coupled windings.

In Fig. 4(a), there will be induced voltages V_{Px} and V_{Nx} in windings *P* and *N* for the *x*-component of the magnetic field $\boldsymbol{B_x(t)}$. Because V_{Px} and V_{Nx} have the same magnitude and polarity, they are a CM voltage $V_{\mathrm{CM}x}$ given by (6). The induced DM voltage $V_{\mathrm{DM}x}$ is zero in (7). For the $\boldsymbol{B_y(t)}$ component in Fig. 4(b), the induced noise voltages V_{PAy} and V_{PBy} in the two winding halves P_A and P_B, respectively, and the induced noise voltages V_{NAy} and V_{NBy} in the two winding halves N_A and N_B, respectively, cancel out, so the induced noise voltages in both windings are zero. For the $\boldsymbol{B_z(t)}$ component in Fig. 4(c), similar to the single-ended inductor winding structure in Fig. 2(c), the winding along the toroidal core has an equivalent winding loop with a radius approximately equal to the core's mean radius. $\boldsymbol{B_z(t)}$ induces a nonzero noise voltage equal to twice that of the induced DM voltage $V_{\mathrm{DM}z}$ in each winding in this equivalent winding loop as given by (8). The induced CM voltage $V_{\mathrm{CM}z}$ is zero in (9)

$$V_{CMx} = (V_{Px} + V_{Nx})/2 = V_{Px} = V_{Nx} \tag{6}$$

$$V_{DMx} = 0 \tag{7}$$

$$2V_{DMz} = V_{Pz} - V_{Nz} = \pi\left(\frac{r_o + r_i}{2}\right)^2 \frac{dB_z(t)}{dt} \tag{8}$$

$$V_{CMz} = 0\,. \tag{9}$$

Based on the above-mentioned analysis, the DM inductors with balanced windings are sensitive to both *x*- and *z*-direction external magnetic field. To reduce the induced voltages, the inductor should be orientated, so the external magnetic field is from *y*-direction, and the radii of the core should be small, so $V_{\mathrm{DM}z}$ can be minimized.

D. Inductor With a Single Twisted Winding

The difference between the conventional single-ended winding inductor and the inductor with a single-ended twisted winding is that the winding of the inductor with a single twisted winding is twisted at 90° and 270° positions as shown in Fig. 5(d). As a result, the twisted winding has an equivalent twisted winding loop as shown in Fig. 5(c).

For convenience, the winding is separated into four parts in Fig. 5. Each part spans 90°. For the *x*-component of the magnetic field $\boldsymbol{B_x(t)}$ in Fig. 5(a), the induced voltages in the four partial windings cancel out, so the total induced voltage is $\mathbf{0}$. For the *y*-component magnetic $\boldsymbol{B_y(t)}$ in Fig. 5(b), the induced voltages in the four partial windings also cancel out, so the total induced voltage is $\mathbf{0}$. For the *z*-component of the magnetic field $\boldsymbol{B_z(t)}$ in Fig. 5(c), different from the single-ended winding structure in Fig. 2(c), because the winding is twisted at 90° and 270° positions, the induced voltages in the four partial windings cancel out, so the total induced voltage is zero.

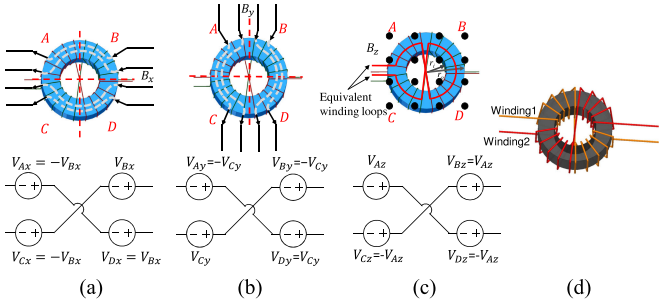

Fig. 6. Induced voltages in a DM inductor with two balanced twisted windings within (a) magnetic field in the *x*-direction, (b) magnetic field in the *y*-direction, (c) magnetic field in the *z*-direction, and (d) structure of a DM inductor with two balanced twisted windings.

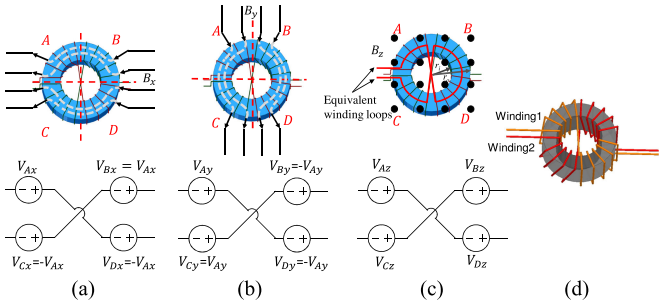

Fig. 7. Induced voltages in a CM inductor with two balanced twisted windings within (a) magnetic field in the *x*-direction, (b) magnetic field in the *y*-direction, (c) magnetic field in the *z*-direction, and (d) structure of a CM inductor with two balanced twisted windings.

Based on this, the DM inductors with a single twisted winding are immune to an even magnetic field. They have much better immunity against the external even magnetic field than the conventional DM inductor with a single-ended winding.

E. DM Inductor With Balanced Twisted Windings

The DM inductor with balanced twisted windings can also be analyzed similarly in Fig. 6. The two balanced, directly coupled windings on this inductor structure have a crossover at 90° and 270°, respectively, as shown in Fig. 6(d). The induced voltages in the four winding parts are the same as those in Fig. 5 for the *x*-, *y*-, and *z*-components. All the induced voltages in the winding parts are canceled out for the *x*-, *y*-, and *z*-components in Fig. 6, so the DM inductor with balanced twisted windings is immune to the external even magnetic field.

Based on this analysis, the DM inductors with a balanced twisted winding are immune to the external even magnetic field and are much better than the conventional DM inductors with balanced two windings.

F. CM Inductor With Balanced Twisted Windings

In Fig. 7, a CM inductor with balanced twisted windings is within a time-varying even magnetic field. The induced voltages in the *x*- and *y*-component magnetic field are 0 because the induced voltages in the four winding parts are canceled out as given in Fig. 7(a) and (b). On the other hand, for the *z*-component magnetic field, because the induced voltages depend on the returning paths of the CM currents, both DM voltage $V_{\mathrm{DM}z}$ and CM voltage $V_{\mathrm{CM}z}$ can be induced as given in (10) and (11), respectively. The total induced voltage across the two windings is $2V_{\mathrm{DM}z}$

$$V_{CMz} = \frac{V_{Az} + V_{Bz} + V_{Cz} + V_{Dz}}{2} \tag{10}$$

$$2V_{DMz} = (V_{Az} + V_{Dz}) - (V_{Bz} + V_{Cz}). \tag{11}$$

Based on the analysis above, compared with conventional CM inductors, after the windings are twisted, the inductors are immune to the *x*- and *y*-direction magnetic field. The induced voltage due to the *z*-direction magnetic field depends on the PCB layout. To reduce this voltage, the two returning paths should be very close to the two equivalent winding paths, respectively, so $V_{\mathrm{CM}z}$ and $V_{\mathrm{DM}z}$ can be minimized.

TABLE I
MAGNETIC FIELD IMMUNITY OF VARIOUS INDUCTORS

Inductor winding structures	X direction	Y direction	Z direction
Single-ended winding inductor	Yes	Yes	No
Single twisted winding inductor	Yes	Yes	Yes
Balanced two-winding CM inductor	No	Yes	Depending on PCB layout
Balanced twisted two winding CM inductor	Yes	Yes	Depending on PCB layout
Balanced two-winding DM inductor	No	Yes	No
Balanced twisted two winding DM inductor	Yes	Yes	Yes

G. Summary

Table I summarizes the immunity performance of the inductors against the external time-varying even magnetic field.

The table shows that twisting an inductor's windings can greatly improve the inductor's immunity to the external magnetic field. For DM inductors, the induced voltage can be eliminated. For CM inductors, the inductor is immune to both *x*- and *y*-direction magnetic field. For the magnetic field from the *z*-direction, the two CM current-returning paths should be very close to the two equivalent winding paths to minimize the induced voltages.

III. EXPERIMENTAL VERIFICATION

The analysis of the induced noise voltages for different inductor winding structures within the time-varying external magnetic field in Section II will be validated with experiments.

In Fig. 8, six inductor prototypes are developed, which are listed as follows:

a) the inductor with single-ended winding;
b) the inductor with single twisted winding;
c) the CM inductor with balanced two windings;
d) the CM inductor with balanced twisted two windings;
e) the DM inductor with two balanced windings;
f) the DM inductor with two balanced twisted windings.

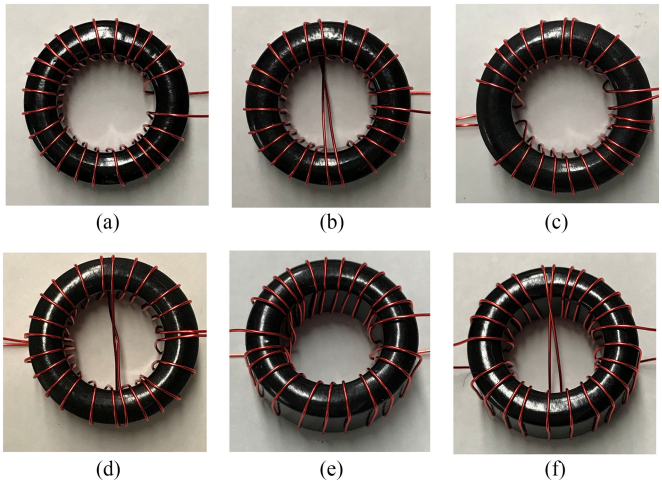

Fig. 8. Inductor prototypes. (a) Inductor with a single-ended winding. (b) Inductor with a single twisted winding. (c) CM inductor with balanced two windings. (d) CM inductor with balanced twisted windings. (e) DM inductor with two balanced windings. (f) DM inductor with two balanced twisted windings.

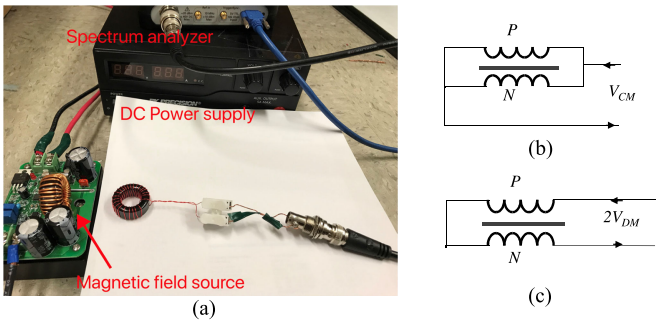

Fig. 9. (a) Measurement setup. (b) Induced CM voltage. (c) Induced DM voltage.

The magnetic cores are powder cores with a relative permeability of 5000. The model number is 35T1000-00 H from Laird-Signal Integrity Products. The inner and outer diameters are 14.23 and 26.67 mm, respectively. The core height is 11 mm. The total number of winding turns is 24. This means, for single-winding inductors, the winding has 24 turns and for two-winding inductors, each winding has 12 turns. The inductance of inductors with single winding is 2.67 mH. The CM inductance of CM inductors with two windings is 637 μH and the DM inductance of DM inductors with two windings is 2.67 mH. AWG #26 wire is used for all inductors.

Fig. 9 shows the measurement setup for the induced CM and DM noise voltages in six inductor prototypes. A dc–dc boost converter with 30 V input voltage and 11.5 A input current is used as the magnetic field source. The major magnetic field is from the boost inductor. The magnetic field is uneven, so it is expected that the induced voltages is reduced, but not fully canceled with twisted windings. All inductors were measured at 30 mm from the boost inductor in Fig. 9. A Tektronix RSA306B spectrum analyzer was used to measure both CM and DM noise voltage spectra induced in the inductor windings. To measure the induced CM voltage in a two-winding inductor, the two

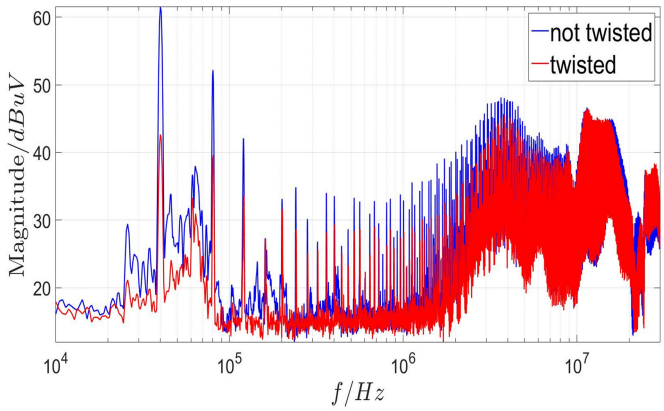

Fig. 10. Induced voltage spectra for the inductors with a single winding.

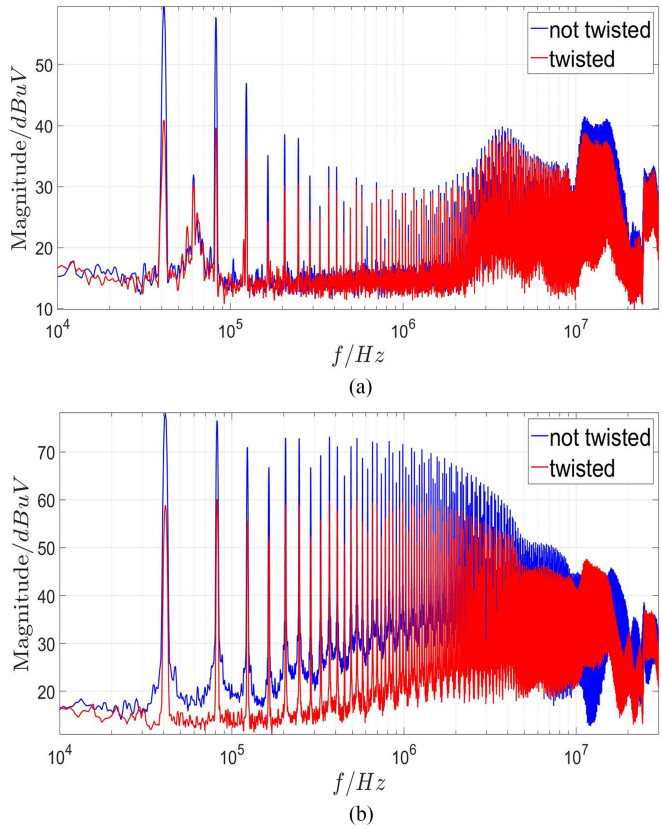

Fig. 11. Induced voltage spectra for CM inductors. (a) CM. (b) DM.

inductor windings were paralleled and the voltage across the two terminals of the paralleled windings was measured in Fig. 9(b). To measure the induced DM voltage in a two-winding inductor, the two inductor windings were in series on one side and the voltage across the two terminals of the series windings on the other side was measured in Fig. 9(c).

Fig. 10 shows the induced voltage in the single-ended twisted winding is 20 dB lower than that in the conventional single-ended winding at the switching frequency 40 kHz. Fig. 11(a) and (b) shows the measurement results for the CM inductors. The induced voltage in the balanced twisted winding is at least 20 dB lower than that in conventional CM inductors for both

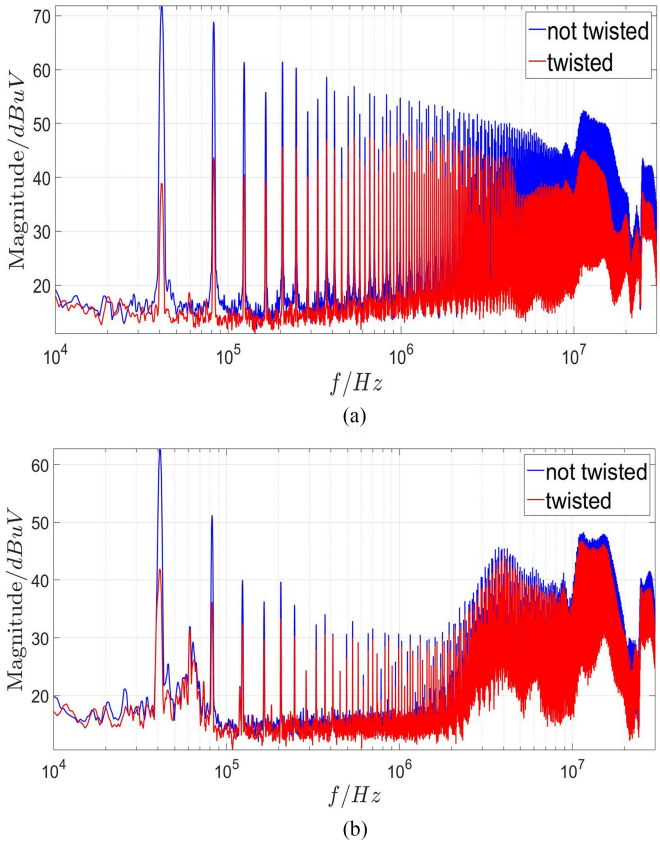

Fig. 12. Induced voltage spectra for two winding DM inductors. (a) CM. (b) DM.

CM and DM. Fig. 12(a) and (b) shows the measurement results for the DM inductors with balanced two windings. The induced voltage in the balanced twisted winding is 33 dB for CM and 20 dB for DM lower than that in conventional DM inductors with balanced two windings at the switching frequency. These measurement results verified the analysis in Section II. The winding-turn distribution along the core will influence the cancelation. If the inductors have evenly distributed winding turns, the cancelation results are the best. Evenly distributed winding turns can be achieved easily with machines, but not by hand. The winding turns in Fig. 8 were not perfectly even as the windings were made by hand. As observed from Figs. 10–12, the cancelation is still very effective. As analyzed in Section II, to achieve a good cancelation, the number of turns of both windings should be the same. In that way, the induced voltages on the two have the same magnitude.

IV. Proposed CM Inductor Structure to Reduce the Induced Voltage and Emitted Near Magnetic Field

In [2], it has been investigated that the inductors generate near magnetic field, so they are also magnetic field noise sources. Twisted windings have been proposed to reduce the emitted near magnetic field. However, in many applications, the leakage inductance of a CM inductor is used as the DM inductance to attenuate the DM noise. When the two windings of a CM inductor are twisted, the DM inductance will be greatly reduced because

TABLE II
Measured Inductor Inductance

Structure types	CM inductance	DM inductance
Single-ended winding inductor	-	2.67 mH
Single twisted winding inductor	-	2.67 mH
Balanced two-winding CM inductor	637 μH	6.37 μH
Balanced twisted two winding CM inductor	637 μH	2.07 μH
Balanced two-winding DM inductor	1.51 μH	2.67 mH
Balanced twisted two winding DM inductor	0.65 μH	2.67 mH

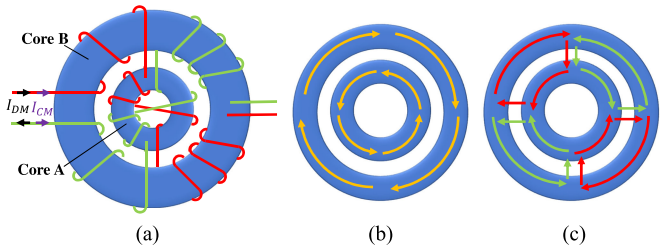

Fig. 13. (a) Proposed CM inductor. (b) CM magnetic flux. (c) DM magnetic flux.

the emitted near magnetic field, which contributes to the leakage inductance of a CM inductor, will be partially canceled. Table II shows the measured DM and CM inductance with a Keysight impedance analyzer E4990A for all inductor prototypes in Section III. It is shown that the twisted windings lead to a greatly reduced DM inductance for CM inductors.

On the other hand, as analyzed in Section III, the twisted windings can help reduce the induced noise voltages within windings in the time-varying external magnetic field. It is therefore a good idea to investigate the immunity of inductors to external magnetic field, the reduction of the emitted near magnetic field from the inductors and the increase of the DM inductance of the CM inductors at the same time.

In this section, a new CM inductor structure is proposed to achieve near magnetic field emission reduction, DM inductance augment, and external magnetic field immunity. The proposed inductor includes two cores in Fig. 13. A small toroidal core A is within a big toroidal core B. The winding structure is shown in Fig. 13(a). Each winding has one twist after a 90° span on each core, so each winding has four winding parts. The CM inductor conducts both CM and DM currents. The magnetic flux paths of the CM current are shown in Fig. 13(b), and the magnetic flux paths of DM current are shown in Fig. 13(c).

The CM fluxes generated by the CM current in the four winding parts on each core enhance inside the core in Fig. 13(b), so a big CM inductance is achieved. The DM fluxes generated by the DM current in the eight winding parts flow between the two cores within the four loops via the air gaps in Fig. 13(c). The leakage DM flux leaked to the air from the four flux loops is small because the flux directions of the adjacent loops are inverse, so they partially cancel out in the air. This reduces the emitted near magnetic field. Although the leakage magnetic field generated by DM currents was greatly canceled with twisted windings in the proposed inductor, because the reluctance of

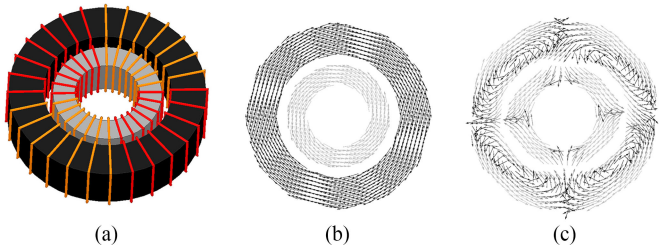

Fig. 14. FEA simulation. (a) 3-D model of the proposed inductor. (b) CM magnetic flux vectors inside the core. (c) DM magnetic flux vectors inside the core.

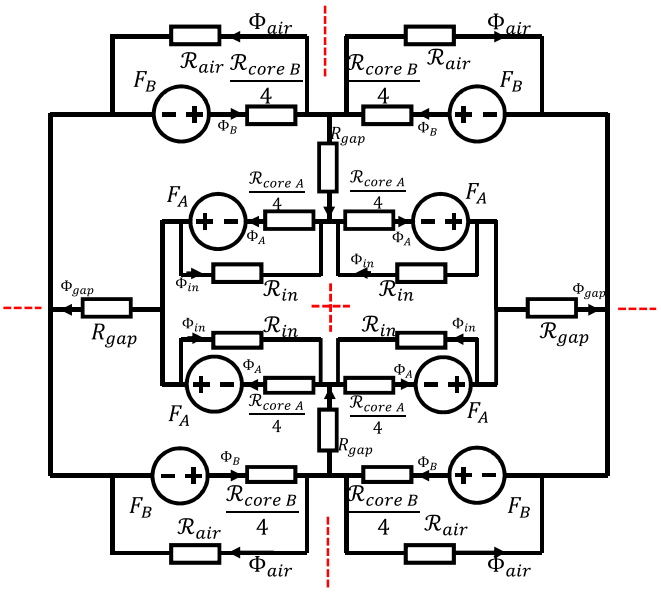

Fig. 15. Magnetic circuit for the proposed CM inductor with the DM current excitation (for the CM current excitation, F_A s and F_B s on the right are reversed).

the four DM flux loops in Fig. 13(c) is much smaller than that of the leakage DM flux loops in the conventional two-winding CM inductors [2], a bigger DM inductance can be achieved. Again, because most of the DM flux is confined within two cores, the emitted near magnetic field is much lower than conventional CM inductors.

To verify the abovementioned flux analysis, a three-dimensional (3-D) finite element analysis (FEA) model was built in Ansys Maxwell 3-D in Fig. 14(a). The orange and red windings represent two windings, respectively. A 90 mA CM current excitation and a 2.1 A DM current excitation were added. The magnetic flux vector distribution on the center *xy* plane of the cores was shown in Fig. 14(b) for the CM current excitation and in Fig. 14(c) for the DM current excitations.

In Fig. 14(b), the CM fluxes are confined in two cores with reversed directions as expected in Fig. 13(b). In Fig. 14(c), the DM fluxes also have the same pattern as expected in Fig. 13(c). Fig. 15 shows the magnetic circuit of the proposed CM inductor with DM current excitation. Because the winding structure is symmetrical, the MMFs generated by the four winding parts on core A are equal. The MMFs generated by the four winding parts on core B are also equal. The magnetic circuit can be

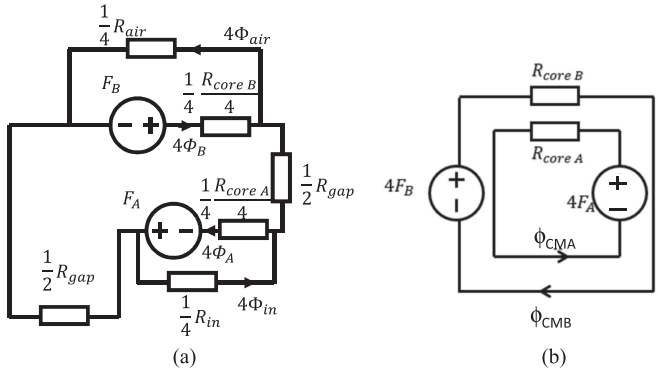

Fig. 16. Reduced magnetic circuit with (a) DM or (b) CM current excitation.

divided into four identical sections as divided by the dashed lines in Fig. 15. The corresponding reluctances in each section are equal. As a result, the magnetic fluxes flowing through the corresponding reluctances are also equal. For the CM current excitation, all F_A s and F_B s in the two sections on the right should be reversed.

In Fig. 15, F_A and F_B represent the MMF generated by the winding parts on core A and core B, respectively. ϕ_A and ϕ_B represent the magnetic flux flowing through the core A and core B, respectively. $\mathcal{R}_{\rm core\,A}$ and $\mathcal{R}_{\rm core\,B}$ represent the reluctance of the entire core A and core B. $\mathcal{R}_{\rm in}$ represents the reluctance of the air, which spans 90° of the inner space of core A, and $\phi_{\rm in}$ represents the flux flowing through it. $\mathcal{R}_{\rm air}$ represents the reluctance of the air, which spans 90° of the outer space of core B, and $\phi_{\rm air}$ represents the magnetic flux flowing through it. $\phi_{\rm air}$ represents the near magnetic field emitted to the air. $\mathcal{R}_{\rm gap}$ represents the equivalent reluctance of the air gap between the two cores in a 90° span, and $\phi_{\rm gap}$ represents the flux flowing through it. Because of the symmetry of the proposed inductor, the magnetic circuit in Fig. 15 can be further reduced to Fig. 16(a). Similarly, the magnetic circuit for the CM current excitation can be reduced to Fig. 16(b).

In Fig. 16(a), the following condition is always satisfied:

$$\mathcal{R}_{\rm core\,A}, \mathcal{R}_{\rm core\,B} \ll \mathcal{R}_{\rm air}, \mathcal{R}_{\rm in}\,. \tag{12}$$

Based on Fig. 16(a), $\phi_{\rm air}$ can be derived as

$$4\phi_{\rm air} \approx \frac{F_B\left(\mathcal{R}_{\rm gap}+\frac{\mathcal{R}_{\rm core\,A}}{16}\right)-F_A\frac{\mathcal{R}_{\rm core\,B}}{16}}{\left(\mathcal{R}_{\rm gap}+\frac{\mathcal{R}_{\rm core\,A}}{16}+\frac{\mathcal{R}_{\rm core\,B}}{16}\right)\times\frac{1}{4}\mathcal{R}_{\rm air}} \tag{13}$$

where

$$\mathcal{R}_{\rm core\,A} = \frac{l_A}{\mu_0\mu_A A_A} \tag{14}$$

$$\mathcal{R}_{\rm core\,B} = \frac{l_B}{\mu_0\mu_B A_B} \tag{15}$$

$$\mathcal{R}_{\rm gap} = \frac{l_{\rm gap}}{\mu_0 A_{\rm gap}} = \frac{r_B - R_A}{\mu_0 A_{\rm gap}} \tag{16}$$

and

$$A_{\rm gap} \approx \frac{\pi\left(r_B+R_A\right)\left(H_B+H_A\right)}{16}\,. \tag{17}$$

In (14) and (15), l_A and l_B represent the effective length of core A and B, respectively; A_A and A_B represent the cross-sectional area of cores A and B, respectively; and μ_A and μ_B represent the relative permeability of cores A and B, respectively. μ_0 is the vacuum's permeability. In (16), r_B represents the inner radius of core B, and R_A represents the outer radius of core A. $l_{\rm gap}$ represents the equivalent length of the air gap between cores A and B, and it can be approximately equal to the difference between r_B and R_A. In (17), H_B and H_A represent the height of cores B and A, respectively. In (16), $A_{\rm gap}$ represents the equivalent cross-sectional area of a 90°-span air gap. It is approximately equal to one-eighth of the cross-sectional area of the whole air gap between the two cores because the average magnetic flux density flowing through the whole air gap is used for $\phi_{\rm gap}$. The fringing effect is ignored since the difference between H_B and H_A, and r_B and R_A is assumed to be small.

From (13), $\phi_{\rm air}$ reduces to zero if the following condition is met:

$$\frac{F_B}{F_A} = \frac{0.5 I_{DM} N_B}{0.5 I_{DM} N_A} = \frac{N_B}{N_A} = \frac{\frac{\mathcal{R}_{\rm core\,B}}{16}}{\mathcal{R}_{\rm gap} + \frac{\mathcal{R}_{\rm core\,A}}{16}}. \tag{18}$$

In (18), N_A and N_B are the total numbers of turns of one winding on cores A and B, respectively. In Fig. 16(a), $\phi_{\rm in}$ has an inverse direction in the air to $\phi_{\rm air}$, so they can partially cancel each other. It should also be noted that $\phi_{\rm in}$ is considered to have little contribution to the near magnetic field emission unless the space close to the center of the inductor is concerned.

For the same reason as in Section II, the proposed inductor with twisted windings on both cores in Fig. 13 is immune to the *x*- and *y*-component external magnetic field. The induced voltage due to the *z*-component external magnetic field can be minimized by aligning the returning path with input and output current paths in Fig. 13(a). This is because, with this returning path layout, the induced voltages due to the *z*-component magnetic field in four winding parts cancel out. So, the proposed CM inductor in Fig. 13 can achieve external magnetic field immunity, greatly reduced near magnetic field emission, and high DM inductance.

For the magnetic circuit with the CM current excitation in Fig. 16(b), ϕ_{CMA} and ϕ_{CMB} are the magnetic flux in cores A and B, respectively. The leakage flux in air and the mutual flux between cores A and B due to the CM current excitation are ignored as most of the magnetic flux is confined within the two cores. The total CM inductance is therefore given by the following equation:

$$L_{\rm CM} = \frac{{N_A}^2}{\mathcal{R}_{\rm core\,A}} + \frac{{N_B}^2}{\mathcal{R}_{\rm core\,B}}. \tag{19}$$

The magnetic fluxes due to the CM current $I_{\rm CM}$ in the two cores are

$$\Phi_{CMA} = \frac{2 N_A I_{CM}}{\mathcal{R}_{\rm core\,A}} \tag{20}$$

$$\Phi_{CMB} = \frac{2 N_B I_{CM}}{\mathcal{R}_{\rm core\,B}}. \tag{21}$$

TABLE III
INDUCTOR PARAMETERS

Inductor structure	Core	Outer diameter	Inner diameter	Height	Turns number	μ_r
Conventional	B	26.67 mm	14.23 mm	11 mm	20	5000
Proposed	A B	16.00 mm 29.00 mm	9.60 mm 19.00 mm	6.3 mm 7.5 mm	N_A=14 N_B=14	4300 40

The magnetic flux densities due to the CM current $I_{\rm CM}$ in the two cores are

$$B_{CMA} = \frac{\Phi_{CMA}}{A_A} \tag{22}$$

$$B_{CMB} = \frac{\Phi_{CMB}}{A_B}. \tag{23}$$

The next step is to design the optimal magnetic flux densities inside cores. In this paper, having the optimal magnetic flux densities inside the two cores, the highest possible magnetic flux density, which is equal to the sum of the flux densities due to DM and CM currents, within the two cores should be larger than half of but smaller than 0.8 times of the saturation flux density of each core at the highest operation temperature. In Fig. 16(a), ignoring the leakage magnetic flux, the magnetic flux due to the DM current $I_{\rm DM}$ is equal in the two cores

$$4\Phi_A = 4\Phi_B = \frac{0.5 N_A I_{DM} + 0.5 N_B I_{DM}}{R_{\rm gap} + \frac{1}{16} R_{\rm core\,A} + \frac{1}{16} R_{\rm core\,B}}. \tag{24}$$

The DM inductance $L_{\rm DM}$ is

$$L_{DM} = \frac{4 \times 0.5 \left(N_A + N_B\right) \Phi_A}{I_{DM}} = \frac{\left(0.5 N_A + 0.5 N_B\right)^2}{R_{\rm gap} + \frac{1}{16} R_{\rm core\,A} + \frac{1}{16} R_{\rm core\,B}}. \tag{25}$$

The magnetic flux densities due to the DM current $I_{\rm DM}$ in two cores are

$$B_{DMA} = \frac{\Phi_A}{A_A} \tag{26}$$

$$B_{DMB} = \frac{\Phi_A}{A_B}. \tag{27}$$

If the saturation flux densities at the highest operation temperature of cores A and B are $B_{{\rm Sat}A}$ and $B_{{\rm Sat}B}$, respectively, to meet the optimal magnetic flux density design, the following equations should be satisfied:

$$0.5 B_{{\rm Sat}\,A} \le B_{DMA} + B_{CMA} \le 0.8 B_{{\rm Sat}\,A} \tag{28}$$

$$0.5 B_{{\rm Sat}\,B} \le B_{DMB} + B_{CMB} \le 0.8 B_{{\rm Sat}\,B}. \tag{29}$$

Equations (18), (19), (28), and (29) can be used to design the proposed CM inductor to achieve the minimized near magnetic field emission due to DM currents, the desired CM inductance, and the optimal magnetic flux densities within the two cores with both DM and CM current excitations. Equation (25) can be used to estimate the DM inductance of the proposed CM inductor.

Table III shows the designed parameters for a conventional CM inductor and the proposed CM inductor based on these

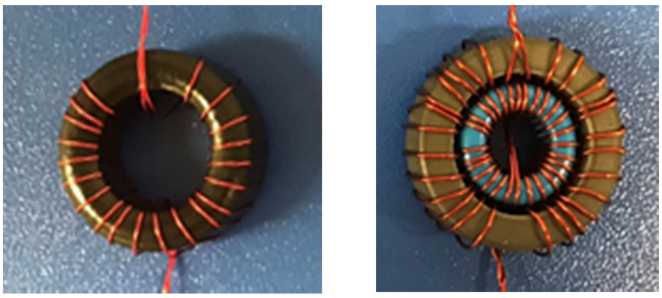

(a) (b)

Fig. 17. Inductor prototypes. (a) Conventional. (b) Proposed.

equations for $I_{\mathrm{DM}_v} = 2.1\,\mathrm{A}$ and $I_{\mathrm{CM}} = 90\,\mathrm{mA}$. $B_{\mathrm{Sat}_A} = B_{\mathrm{Sat}_B} = 0.2\,\mathrm{T}$ at 100 °C. All the inductors were designed to have identical CM inductance $L_{\mathrm{CM}} = 557\,\mu\mathrm{H}$.

Fig. 17 shows the inductor prototypes. Due to the availability of magnetic cores, the outer core B of the proposed inductor has a larger diameter than the core of the conventional CM inductor. However, the core of the conventional inductor has a bigger height than those of the proposed CM inductor. The winding wire size is AWG #22.

V. Experimental Verification

A. Induced Noise Voltage Measurement

The induced DM and CM voltages in the CM inductor prototypes developed in Table III and Fig. 17 were tested with the same setup as in Fig. 9.

The measured results are shown in Fig. 18. The proposed CM inductor can reduce the induced CM noise voltage by more than up to 27 dB, a factor of 22 times at low frequencies and reduce the induced DM noise voltage by more than up to 55 dB, a factor of 560 times, within a wide frequency range than the conventional CM inductor.

B. Near Magnetic Field Measurement

The emitted near magnetic field was measured with a signal generator RIGOL DG4062, a Beehive Electronics 100 C EMC probe, an Amplifier Research Model 25A250A amplifier, and a Rohde & Schwarz FSH4 spectrum analyzer. A 200 kHz, 1.4 A sinusoidal current was applied to the inductors. The measurement setup is shown in Fig. 19. A 20 cm × 20 cm coordinate board with a 7 × 7 grid is 25 mm above the inductors.

The Beehive EMC probe was used to measure the magnetic flux density B_x in the x-direction, B_y in the y-direction, and B_z in the z-direction at each point on the grid. The measured data were exported from the spectrum analyzer to a PC to calculate the composite magnetic flux density B according to the following equation:

$$B = \sqrt{B_x^2 + B_y^2 + B_y^2}\,. \tag{30}$$

The measurement results are shown in Fig. 20. As the comparison shown in the figure, the proposed CM inductor can greatly reduce the near magnetic field emission by more than 80%.

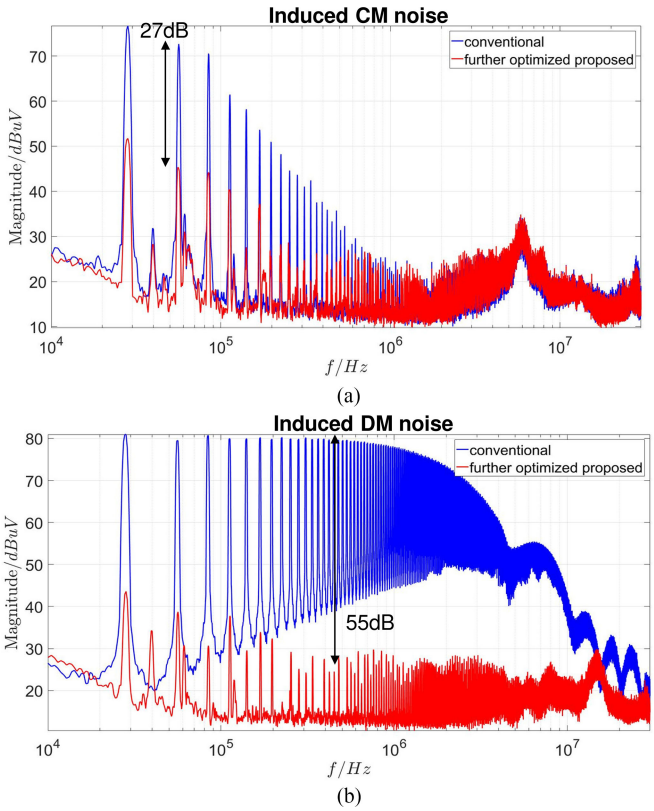

Fig. 18. Comparison of the induced voltage spectra of CM inductors. (a) CM noise. (b) DM noise.

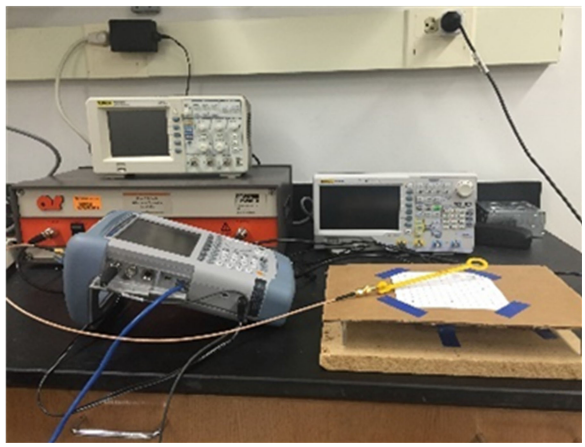

Fig. 19. Near magnetic field measurement setup.

The experimental results verified the analysis in the previous sections.

C. Impedance Measurement

The impedance of the inductors was measured with a Keysight impedance analyzer E4990A. The measurement results are given in Fig. 21. It is given in Fig. 21(a) that the two CM inductors have the almost the same CM impedance with a CM inductance $L_{\mathrm{CM}} = 557\,\mu\mathrm{H}$ at low frequencies.

In Fig. 21(b), the proposed CM inductor has a DM inductance of 8.9 μH, which is much higher than the DM inductance

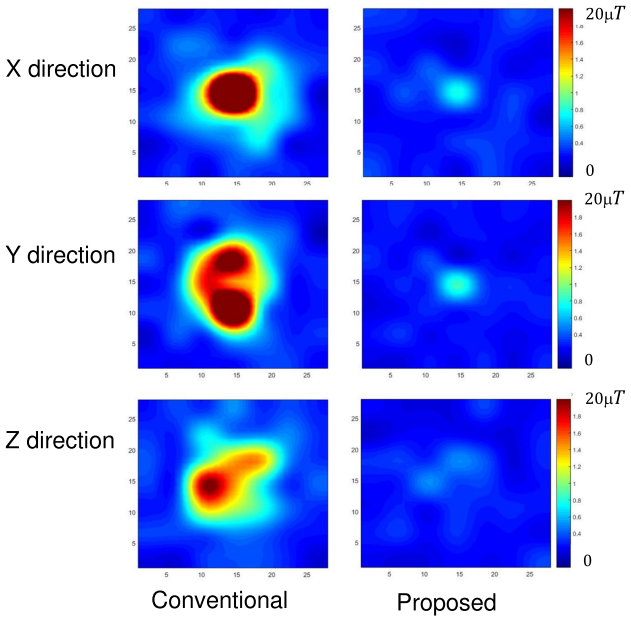

Fig. 20. Comparison of the measured near magnetic field emission of a conventional inductor and a proposed inductor in *x*-, *y*-, and *z*-directions.

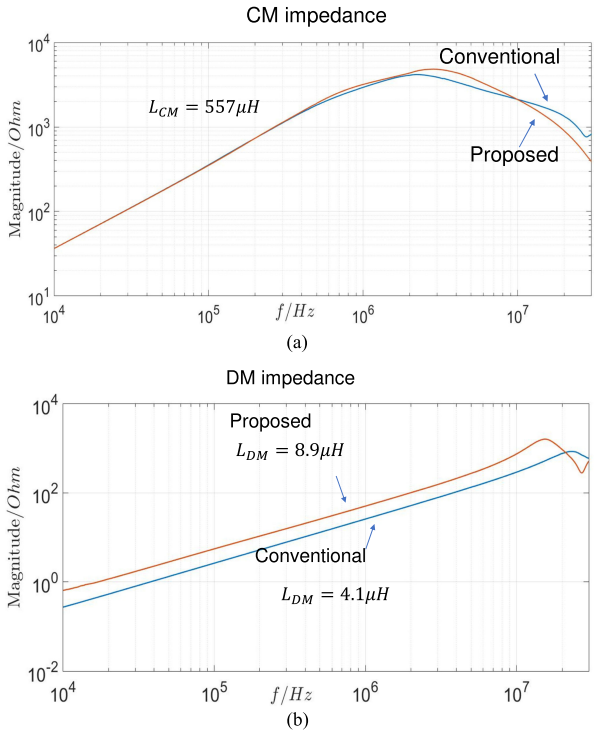

Fig. 21. Comparison of the measured impedance. (a) CM impedance. (b) DM impedance.

of 4.1 μH from the conventional CM inductor. This validated that the proposed CM inductor can greatly increase the DM inductance.

D. In-Circuit EMI Measurement

The two inductors were used as the inductor of an input π-type EMI filter of a dc/dc boost converter. Two CM capacitors

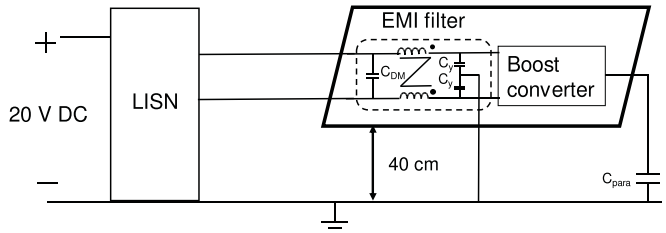

Fig. 22. EMI measurement setup with inductors used as filter inductors in a boost converter.

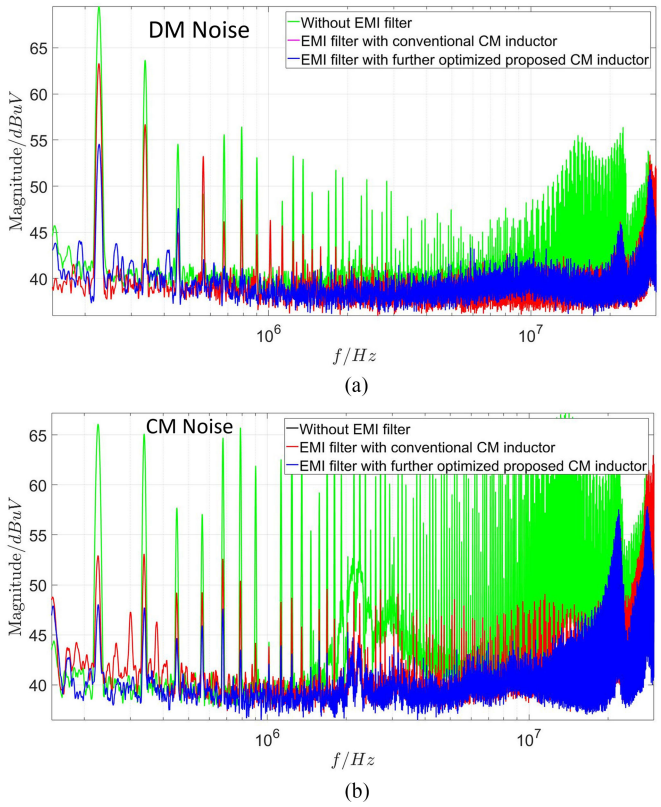

Fig. 23. Comparison of the measured EMI with inductors used as filter inductors in a boost converter. (a) DM noise. (b) CM noise.

C_y have the capacitance of 680 pF; and the DM capacitor C_{DM} is 0.47 μF. The input current of the converter is 2 A. It is expected that the proposed inductor can help the EMI filter to achieve a better performance than the conventional inductor because it is immune to the external magnetic field generated by the other components in the converter and it does not emit the near magnetic field to contaminate other filter components. Fig. 22 shows the measurement setup.

The comparison of the measured DM and CM noise is shown in Fig. 23.

In Fig. 23, green curves are the noise without EMI filters. Red curves are the EMI using the EMI filter with the conventional CM inductor. Blue curves are the EMI using the EMI filter with the proposed CM inductor. It is shown that compared with the conventional CM inductor, the proposed CM inductor can further reduce the DM noise by up to 15 dB from 150 kHz to 2 MHz, and the CM noise by up to 12 dB from 150 kHz to

15 MHz. This further validated the proposed technique. It is expected that the actual EMI reduction performance with the proposed CM inductor depends on the distribution of the near magnetic field in the converter, the component layout and the magnitude of the conductive EMI.

It should be pointed out that, although the proposed CM inductor uses longer winding wires and one more core, the EMI filter with the conventional CM inductor needs more filter components such as inductors or capacitors, to achieve the same performance as the filter with the proposed inductor. As a result, the footprint, power loss, and the cost of the filter with the conventional inductor may be higher than that with the proposed inductor. Due to the limited space of this paper, it cannot be given in detail. The measured actual temperature rising difference between the proposed CM inductor and the conventional CM inductor is less than 2 °C.

It should also be pointed out that the proposed CM inductor structure can be easily implemented using the two individual concentric inductors with their winding terminals soldered to a PCB. The two inductors do not need to be directly connected using winding wires. They can be connected using PCB traces.

VI. Conclusion

In this paper, the induced noise voltages in different inductor winding structures due to external near magnetic field are investigated. The mechanism of the noise voltage induction in different inductor winding structures is analyzed and the equivalent circuits are developed. Experiments are carried out to verify the developed theory. A CM inductor structure is proposed to achieve a minimized near magnetic field emission, a high immunity against the external magnetic field, and a greatly increased DM inductance. Furthermore, the technique to design an optimal magnetic flux density inside cores of the proposed inductors is developed. The prototypes are built and experiments are carried out to validate the developed technique.

References

[1] R. Lai, Y. Maillet, F. Wang, S. Wang, R. Burgos, and D. Boroyevich, "An integrated EMI choke for differential-mode and common-mode noise suppression," *IEEE Trans. Power Electron.*, vol. 25, no. 3, pp. 539–544, Mar. 2010.

[2] B. Zhang and S. Wang, "Analysis and reduction of the near magnetic field radiation from magnetic inductors," in *Proc. IEEE Appl. Power Electron. Conf. Expo.*, Tampa, FL, USA, 2017, pp. 2494–2501.

[3] Y. Chu, S. Wang, N. Zhang, and D. Fu, "A common mode inductor with external magnetic field immunity, low-magnetic field emission, and high-differential mode inductance," *IEEE Trans. Power Electron.*, vol. 30, no. 12, pp. 6684–6694, Dec. 2015.

[4] W. Tan, C. Cuellar, X. Margueron, and N. Idir, "A common-mode choke using Toroid-EQ mixed structure," *IEEE Trans. Power Electron.*, vol. 28, no. 1, pp. 31–35, Jan. 2013.

[5] Y. Chu, S. Wang, J. Xu, and D. Fu, "EMI reduction with near field coupling suppression techniques for planar transformers and CM chokes in switching-mode power converters," in *Proc. IEEE Energy Convers. Congr. Expo.*, Denver, CO, USA, 2013, pp. 3679–3686.

[6] S. Wang, F. C. Lee, and W. G. Odendaal, "Using scattering parameters to characterize EMI filters," in *Proc. IEEE 35th Annu. Power Electron. Specialists Conf.*, 2004, pp. 297–303.

[7] S. Wang, P. Kong, and F. C. Lee, "Common mode noise reduction for boost converters using general balance technique," *IEEE Trans. Power Electron.,* vol. 22, no. 4, pp. 1410–1416, Jul. 2007.

[8] S. Wang, R. Chen, J. D. Van Wyk, F. C. Lee, and W. G. Odendaal, "Developing parasitic cancellation technologies to improve EMI filter performance for switching mode power supplies," *IEEE Trans. Electromagn. Compat.*, vol. 47, no. 4, pp. 921–929, Nov. 2005, ISSN 0018-9375.

[9] S. Wang, F. C. Lee, and J. D. van Wyk, "Design of inductor winding capacitance cancellation for EMI suppression," *IEEE Trans. Power Electron.*, vol. 21, no. 6, pp. 1825–1832, Nov. 2006, ISSN 0885-8993.

[10] S. Wang, F. C. Lee, D. Y. Chen, and W. G. Odendaal, "Effects of parasitic parameters on EMI filter performance," *IEEE Trans. Power Electron.*, vol. 19, no. 3, pp. 869–877, May 2004.

[11] S. Wang, F. C. Lee, and J. D. van Wyk, "Inductor winding capacitance cancellation using mutual capacitance concept for noise reduction application," *IEEE Trans. Electromagn. Compat.*, vol. 48, no. 2, pp. 311–318, May 2006.

[12] S. Wang, F. C. Lee, and W. G. Odendaal, "Cancellation of capacitor parasitic parameters for noise reduction application," *IEEE Trans. Power Electron.*, vol. 21, no. 4, pp. 1125–1132, Jul. 2006.

[13] F. S. F. Silva *et al.*, "High gain dc–dc boost converter with a coupling inductor," in *Proc. Brazilian Power Electron. Conf.*, 2009, pp. 486–492.

[14] H. Zhang, B. Zhang, and S. Wang, "Integrated common mode and differential mode inductors with low near magnetic field emission," in *Proc. IEEE Energy Convers. Congr. Expo.*, Cincinnati, OH, USA, 2017, pp. 5375–5382.

[15] H. Zhang, S. Wang, and Q. Wang, "Winding and air gap configurations for power inductors to reduce near magnetic field emission," in *Proc. IEEE Energy Convers. Congr. Expo.*, Cincinnati, OH, USA, 2017, pp. 903–910.

[16] M. J. Nave, "On modeling the common mode inductor," in *Proc. IEEE Int. Symp. Electromagn. Compat.*, Cherry Hill, NJ, USA, 1991, pp. 452–457.

[17] D. J. Wilcox, M. Conlon, and W. G. Hurley, "Calculation of self and mutual impedances for coils on ferromagnetic cores," *IEE Proc. A—Physical Sci., Meas. Instrum., Manage. Educ.—Rev.*, vol. 135, no. 7, pp. 470–476, Sep. 1988.

[18] F. C. Lee, J. D. van Wyk, Z. X. Liang, R. Chen, S. Wang, and B. Lu, "An integrated power electronics modular approach: Concept and implementation," in *Proc. The 4th Int. Power Electron. Motion Control Conf.*, Xi'an, China, 2004, pp. 1–13.

[19] Y. Lai and S. Wang, "Investigation of magnetic field immunity and near magnetic field reduction for the inductors in high power density design," in *Proc. IEEE Appl. Power Electron. Conf. Expo.*, San Antonio, TX, USA, 2018, pp. 587–594.

[20] S. Wang, F. C. Lee, and W. G. Odendaal, "Single layer iron powder core inductor model and its effect on boost PFC EMI noise," in *Proc. IEEE 34th Annu. Conf. Power Electron. Specialist*, 2003, pp. 847–852.

[21] A. Lemmon, R. Cuzner, J. Gafford, R. Hosseini, A. D. Brovont, and M. Mazzola, "Methodology for characterization of common-mode conducted electromagnetic emissions in wide-bandgap converters for ungrounded shipboard applications," *IEEE J. Emerg. Sel. Topics Power Electron.*, vol. 6, no. 1, pp. 300–314, Mar. 2018.

[22] A. Hariya *et al.*, "Circuit design techniques for reducing the effects of magnetic flux on GaN-HEMTs in 5-MHz 100-W high power-density LLC resonant dc–dc converters," *IEEE Trans. Power Electron.*, vol. 32, no. 8, pp. 5953–5963, Aug. 2017.

[23] R. Wang, H. F. Blanchette, M. Mu, D. Boroyevich, and P. Mattavelli, "Influence of high-frequency near-field coupling between magnetic components on EMI filter design," in *Proc. 28th Annu. IEEE Appl. Power Electron. Conf. Expo.*, 2013, pp. 4568–4579.

[24] T. Chen, "*Inductor design for common-mode and differential mode inductors*," M.S thesis, Dept. Elect. and Comput. Eng., Univ. Texas, San Antonio, TX, USA, 2014.

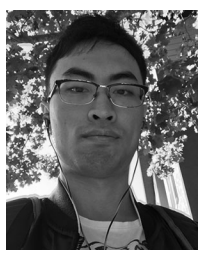

Yanwen Lai received the B.E. degree in electrical engineering from the South China University of Technology, Guangzhou, China, in 2016 and the M.S. degree from the University of Florida, Gainesville, FL, USA, in 2018.

He was a Research Assistant in power electronics at the Electrical Power Research Laboratory. His research interests include power electronics and electromagnetic interference.

Shuo Wang (S'03–M'06–SM'07) received the Ph.D. degree from Virginia Tech, Blacksburg, VA, USA, in 2005.

From 2005 to 2009, he was a Research Assistant Professor with Virginia Tech. From 2009 to 2010, he was a Senior Design Engineer with GE Aviation Systems, Vandalia, USA. From 2010 to 2014, he was with the University of Texas, San Antonio, TX, USA, first as an Assistant Professor and later as an Associate Professor. Since 2015, he has been an Associate Professor with the Department of Electrical and Computer Engineering, University of Florida, Gainesville, FL, USA. He has authored or coauthored more than 160 IEEE journal and conference papers and holds eight US patents.

Dr. Shuo Wang received the Best Transaction Paper Award from the IEEE Power Electronics Society in 2006, and the William M. Portnoy Award twice for the papers published in the IEEE Industry Applications Society, in 2004 and 2012, respectively. In 2012, he received the prestigious National Science Foundation CAREER Award. He is an Associate Editor for the IEEE TRANSACTIONS ON INDUSTRY APPLICATIONS and a technical program Co-Chair for IEEE 2014 International Electric Vehicle Conference.

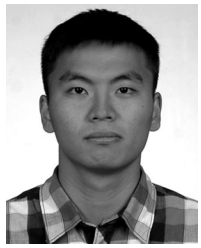

Boyi Zhang (S'17) received the B.S. degree in electrical engineering from the Harbin Institute of Technology, Harbin, China, in 2015, and the M.S. degree in electrical engineering from the University of Florida, Gainesville, FL, USA, in 2017. He is currently working toward the Ph.D. degree in power electronics at the electrical power research lab, University of Florida.

His research interests include power electronics, electromagnetic interference, magnetic components, and wide bandgap power device packaging.

Mr. Zhang received the Best Student Presentation Award in the Applied Power Electronics Conference (APEC) 2017, held in Tampa, FL, USA.